







RESEARCH ARTICLE | OCTOBER 25 2023

The evolution of a three-dimensional microbubble at a corner in a Maxwell fluid ^{EP}

Special Collection: [Tanner: 90 Years of Rheology](#)

E. N. O'Brien   ; M. Mahmud (مهدي حسن محمود)  ; W. R. Smith  ; Q. X. Wang (汪前喜)  ; T. N. Phillips 

 Check for updates

Physics of Fluids 35, 103120 (2023)

<https://doi.org/10.1063/5.0170820>



View
Online



Export
Citation

CrossMark



APL Quantum
Bridging fundamental quantum research with technological applications

Now Open for Submissions
No Article Processing Charges (APCs) through 2024

Submit Today



The evolution of a three-dimensional microbubble at a corner in a Maxwell fluid

Cite as: Phys. Fluids **35**, 103120 (2023); doi: [10.1063/5.0170820](https://doi.org/10.1063/5.0170820)

Submitted: 4 August 2023 · Accepted: 5 October 2023 ·

Published Online: 25 October 2023



View Online



Export Citation



CrossMark

E. N. O'Brien,^{1,a)}  M. Mahmud (مهدي حسن محمود),²  W. R. Smith,¹  Q. X. Wang (汪前喜),¹  and T. N. Phillips³ 

AFFILIATIONS

¹School of Mathematics, University of Birmingham, Birmingham B152TT, United Kingdom

²Department of Mathematics, College of Science, Salahaddin University-Erbil, Erbil, Iraq

³School of Mathematics, Cardiff University, CF244AG, Cardiff, United Kingdom

Note: This paper is part of the special topic, Tanner: 90 Years of Rheology.

^{a)} Author to whom correspondence should be addressed: exo219@bham.ac.uk

ABSTRACT

Bubbles often appear in non-Newtonian liquids from nature, engineering to biomedical applications, but their study has been under research compared to their Newtonian counterpart. Here, we extend the axisymmetric modeling of Lind and Phillips to three-dimensional modeling. The approach is based on the boundary integral method coupled with the Maxwell constitutive equation. The flow is assumed to have moderate to high Reynolds numbers and, thus, is irrotational in the bulk domain. The viscoelastic effects are incorporated approximately in the normal stress balance at the bubble surface. The numerical model has excellent agreement with the corresponding Rayleigh–Plesset equation for spherical bubbles in a non-Newtonian liquid. Computations are carried out for a bubble near a corner at various angles. The numerical results agree very well with the experiments for bubbles in a Newtonian fluid in a corner. As the Deborah number increases, the amplitude and period of the bubble oscillation increase, the bubble migration to the corner enhances, and the bubble jet is broader, flatter, and inclined more to the further boundary. This implies an improvement to surface cleaning of all surrounding boundaries for ultrasonic cavitation cleaning and results in greater administration of noninvasive therapy and drug delivery.

© 2023 Author(s). All article content, except where otherwise noted, is licensed under a Creative Commons Attribution (CC BY) license (<http://creativecommons.org/licenses/by/4.0/>). <https://doi.org/10.1063/5.0170820>

I. INTRODUCTION

Bubbles in non-Newtonian fluids are widely encountered in various domains such as decompression sickness,¹ volcanic eruption,² glass manufacture, materials, petrochemicals, metallurgy, and different dispersed systems.³ Certain additions of polymers have been reported to affect cavitation damage^{4–6} and noise.⁷

Biomedical applications include nondestructive medical imaging,⁸ extracorporeal shock wave lithotripsy,⁹ treatment of kidney stones,¹⁰ and noninvasive therapy and drug delivery.^{11–14} The non-Newtonian properties of the fluid are important due to the rheological properties of the blood and other bodily fluids.^{15,16}

The behavior of viscoelastic fluids is characterized by performing experiments in the laboratory using a rheometer. Examples of simple flows that are studied include simple shear flow, extensional flow, and oscillatory shear flow. The latter is used to determine the relaxation times of the fluid, a key measure of the viscoelastic nature of the fluid. There are two classes of fluids that often display Maxwell-like behavior in the normal measuring range ($10^{-2} - 10^2$ Hz) with the expected

shapes of the curves for the storage and loss moduli and a single relaxation time. (Note that this frequency range refers to the experiments conducted by the rheometer and not the oscillatory frequency of the bubble.) These are associative thickener-type polymers [e.g., hydrophobic ethoxylated urethane (HEUR)]¹⁷ and worm-like surfactant micellar systems (e.g., aqueous surfactant solutions containing thread-like micelles).^{18–20} Fluids in the latter class are sometimes called “living polymers” because if they break under large stresses, they can reconstitute under conditions of rest or low stress.

Extensive research has been developed for bubbles in a Newtonian fluid.^{21,22} One of the computational models that has been used widely in bubble simulations is the boundary integral method (BIM) based on a potential flow theory for inertially dominant flows.^{23,24} The BIM is accurate and efficient in modeling three-dimensional complex bubble dynamics and its interaction with rigid, free, and elastic boundaries.^{25–29} Weak viscous effects are approximated in this model using the viscous pressure correction, which is determined by the conservation of energy at the interface.^{30,31}

Bubble dynamics were also simulated based on the Navier–Stokes equations using the finite volume method (FVM)^{32–36} or finite element method.^{37,38} These are mainly for axisymmetric profiles.

Contrary to Newtonian bubble dynamics, investigations on bubbles in non-Newtonian fluids have been sparse. A rising bubble in a non-Newtonian fluid was observed experimentally by Wagner *et al.*³⁹ This was numerically simulated by Lind and Phillips,⁴⁰ using the BIM along with Maxwell’s constitutive equation. Lind and Phillips⁴¹ also simulated bubbles near a free surface. Liu *et al.*⁴² computed equally spaced bubbles rising in a viscoelastic fluid.

Recent developments have focused on a three-dimensional bubble rising in a viscoelastic fluid,^{43,44} with particular emphasis on predictions of the velocity discontinuity at critical volume.^{45,46} However, the domain still remains radially symmetric, and three-dimensional effects are scarcely analyzed.

In Secs. II and III, we extend the axisymmetric viscoelastic BIM of Lind and Phillips^{40,41,47} to three-dimensional modeling. The viscoelastic liquid is modeled using the Maxwell constitutive equation. The flow is assumed to have moderate to high Reynolds numbers and, thus, is irrotational in the bulk domain. The viscoelastic effects are approximately included in the normal stress balance at the bubble surface. In Sec. IV, the numerical model is validated by comparing with the corresponding Rayleigh–Plesset equation for spherical bubbles in a non-Newtonian liquid and experiments for bubbles in Newtonian fluid in a corner. In Sec. V, computations are performed for a bubble near a corner at various corner angles using Green’s function for Laplace’s equation in the corner domain. Viscoelastic effects are studied in terms of the Deborah number *De*. In Sec. VI, some conclusions are made with reference to the bubble radius amplitude, oscillation period, migration to the corner, Kelvin impulse, and bubble jet profile.

II. PHYSICAL AND MATHEMATICAL MODEL

We consider a bubble in a viscoelastic fluid located near a corner formed by two rigid flat boundaries. We assume that the associated liquid flow has moderate to high Reynolds numbers, and thus, viscoelastic effects are negligible in the bulk. The viscoelastic effects are not negligible in a thin viscous layer at the bubble surface, which is approximated only through the normal stress balance. Viscous fluid dynamics can be described approximately by potential flows when the vorticity is small or is confined to a narrow layer near the boundary.⁴⁸ It is particularly useful for a gas–liquid two-phase flow with an interface.

Assuming that the flow is irrotational and incompressible in the bulk, the velocity, $\mathbf{u}^* = \nabla^* \phi^*$ satisfies Laplace’s equation in the fluid given by

$$\nabla^{*2} \phi^* = 0. \tag{1}$$

The kinematic boundary conditions on the two rigid boundaries, S_W , the bubble surface S_B , and the far field are given, respectively, by

$$\frac{\partial \phi^*}{\partial n} = 0 \text{ on } S_W, \tag{2}$$

$$\frac{D\mathbf{r}_p^*}{Dt^*} = \nabla^* \phi^* \text{ on } S_B, \tag{3}$$

$$\nabla \phi^* = 0 \text{ as } \mathbf{r}^* \rightarrow \infty, \tag{4}$$

where \mathbf{r}_p^* is a material point at the bubble surface and \mathbf{r}^* is a field point.

At any instant in time, the fluid pressure at the bubble surface is related to the bubble pressure and viscoelastic effects, through the normal stress balance^{40,47}

$$P_L^* + P_{vc}^* = P_B^* - 2\sigma\kappa^* + T_{nn}^*, \tag{5}$$

where P_L^* is the liquid pressure on the bubble surface, σ is the surface tension coefficient, κ^* is the curvature of the bubble surface, P_B^* is the internal pressure of bubble gases, and T_{nn}^* represents the component of deviatoric stress on the bubble surface. Here, P_{vc}^* is proportional to the normal stress T_{nn}^* induced by the irrotational velocity $P_{vc}^* = -CT_{nn}^*$ where the constant *C*, given by Manmi and Q. Wang,³⁰ is

$$C = \frac{\int_S \nabla^* \phi^* \cdot \frac{\partial \nabla^* \phi^*}{\partial n} dS}{\int_S \frac{\partial \phi^*}{\partial n} \frac{\partial^2 \phi^*}{\partial n^2} dS} - 1. \tag{6}$$

Maxwell’s constitutive equation is used to model the non-Newtonian properties of the fluid. The equation yields a general irrotational equation of motion and provides no contribution to stress in the bulk⁴⁹ and so the viscoelastic effects only appear in the normal stress balance condition. However, the model comes with the limitation of only being applicable for small deformations.⁵⁰ Thus, a “material” Maxwell model is used. The material Maxwell model means that the material time derivative collapses to a time derivative in the particle reference frame and can, therefore, be easily calculated.⁴⁰

The Maxwell model can be applicable based on the following reasons: the bubble is approximately spherical during most of its lifetime due to surface tension. It may become non-spherical during a very short period at the end of collapse when the inertial effects are dominant and the viscoelastic effects are negligible. In addition, as for the moderate Reynolds number Newtonian case, jet formation is completely suppressed in the case of a bubble in a viscoelastic fluid near a rigid boundary.⁵¹ Jet suppression has also been seen experimentally in viscoelastic fluids.^{52,53}

Maxwell’s constitutive equation is given by⁵⁴

$$\lambda_1 \frac{DT_{nn}^*}{Dt^*} + T_{nn}^* = 2\mu_L \frac{\partial^2 \phi^*}{\partial n^2}, \tag{7}$$

where λ_1 is the relaxation time of the fluid.

For general constitutive equations, we cannot find a function ψ that satisfies $\nabla \cdot \mathbf{T} = \nabla \psi$ for general irrotational flows.⁴⁹ In these situations, we have $\nabla \times \nabla \cdot \mathbf{T} \neq 0$ even though $\nabla \times \mathbf{u} = 0$, for velocity \mathbf{u} . We cannot always find a function ψ satisfying the above equation so that not all fluids will satisfy a Bernoulli equation. However, under the assumptions described above, the admissibility condition can be satisfied in an approximate sense for moderate to large Reynolds numbers since $\nabla \cdot \mathbf{T}$ becomes small compared to inertial terms in the momentum equation in the bulk of the flow.⁴⁷ Hence, a Bernoulli equation is admissible for inviscid Newtonian, viscous Newtonian, and linear Maxwell fluids with appropriate Reynolds numbers, where $\psi = 0$. Therefore, under such a condition, the potential flow theory can accurately provide a three-dimensional description for a bubble in a Maxwell fluid.

Assuming that the gas-bubble is adiabatic, the pressure inside the bubble is given by

$$P_B^* = P_v + P_g = P_v + P_{g0} \left(\frac{V_0}{V} \right)^\zeta, \quad (8)$$

where P_{g0} is the initial partial pressure of the gas, V_0 is the initial volume of the bubble, and ζ is the heat capacity ratio.

Using Bernoulli's equation for the velocity potential and equation (5), we obtain

$$\rho \frac{D\phi^*}{Dt^*} = \frac{\rho}{2} |\nabla^* \phi^*|^2 - \rho g z^* - P_v + P_{g0} \left(\frac{V_0}{V} \right)^\zeta - 2\sigma \kappa^* + T_{mm}^* + P_0, \quad (9)$$

where ρ is the density of the surrounding fluid, g is the gravitational constant, and P_0 is the ambient pressure of the fluid surrounding the bubble.

From now on the non-spherical bubble model is converted into a nondimensional problem with the length scale being the initial bubble radius R_0 and the pressure scale being $P_0 - P_v$. The stand-off distances, γ_N and γ_F , are the normalized distances between the bubble center and the near and far wall, respectively. Hence, we obtain the dimensionless model for the non-spherical bubble

$$\mathbf{u}|_{S_B} = \frac{D\mathbf{r}_p}{Dt} = \nabla \phi|_{S_B}, \quad (10)$$

$$\frac{D\phi}{Dt} = 1 + \frac{1}{2} |\nabla \phi|^2 - \delta^2 z - \varepsilon \left(\frac{V_0}{V} \right)^\zeta + \frac{2\kappa}{We} - \frac{2C}{Re} \frac{\partial^2 \phi}{\partial n^2} - T_{mm}, \quad (11)$$

$$De \frac{DT_{mm}}{Dt} + T_{mm} = \frac{2}{Re} \frac{\partial^2 \phi}{\partial n^2}, \quad (12)$$

where $\delta = \sqrt{gR_m \rho / (P_\infty - P_v)}$ is the buoyancy parameter, $\varepsilon = P_{g0} / (P_0 - P_v)$ is a measure of the initial bubble gas pressure, $We = R_0 (P_0 - P_v) / \sigma$ is the Weber number measuring the effect of surface tension,⁵⁶ and $Re = R_0 \sqrt{(P_0 - P_v) \rho} / \mu_L$ is the Reynolds number.³⁰ The Deborah number, De , of the fluid is given by⁵⁷

$$De = \frac{\lambda_1}{R_0} \left(\frac{P_0 - P_v}{\rho} \right)^{\frac{1}{2}}. \quad (13)$$

We note that as λ_1 approaches zero, that is, the relaxation time of the fluid becomes instantaneous, De also approaches zero, and the Maxwell model reverts back to the Newtonian model.

III. NUMERICAL MODEL

The initial mesh is first approximated using an icosahedron with 20 equal-sized triangles and 12 nodes situated on a spherical bubble surface. The mesh is then improved by dividing each triangle into four smaller triangles with new nodes added at the midpoint of each line segment and projected onto the surface of a sphere. On each triangular element, the field point, \mathbf{r} , velocity potential, ϕ , and normal velocity, $\partial\phi/\partial n$, are linearly interpolated.²⁵

A high-quality surface mesh of the bubble surface is maintained by implementing a hybrid of the Lagrangian method and elastic mesh technique.⁵⁸ The bubble surface and potential distribution were interpolated using a polynomial scheme coupled with the moving least squares method for calculating the surface curvature and tangential velocity on the surface.^{59,60}

The boundary integral method (BIM) can be implemented with Green's second identity given by

$$c(\mathbf{r}, t) \phi(\mathbf{r}, t) = \int_{\partial\Omega} \left(\frac{\partial\phi(\mathbf{q}, t)}{\partial n} G(\mathbf{r}, \mathbf{q}) - \phi(\mathbf{q}, t) \frac{\partial G(\mathbf{r}, \mathbf{q})}{\partial n} \right) dS, \quad (14)$$

where $c(\mathbf{r}, t)$ is the solid angle, \mathbf{n} is the unit outward facing normal at the surface, and $\partial\Omega$ represents every boundary in the domain, Ω . For a corner angle of π/k , for some natural number, k , Green's function is given by

$$G(\mathbf{r}, \mathbf{q}) = \sum_{j=0}^{2k-1} \frac{1}{|\mathbf{r} - \mathbf{q}_j|}, \quad (15)$$

where \mathbf{q}_0 is the source point and \mathbf{q}_j are the image points of \mathbf{q}_0 for $j = 1, 2, \dots, 2k - 1$. The images were provided by Kucera and Blake⁶¹ and Tagawa and Peters.⁶² A proof is provided by Wang *et al.*⁶³

To calculate the normal stress, T_{mm} , we need to calculate $\partial^2 \phi / \partial n^2$. This is calculated using the following equation:

$$\frac{\partial^2 \phi}{\partial n^2} = \mathbf{n} \cdot \frac{\partial}{\partial n} \nabla \phi = n_x \frac{\partial \phi_x}{\partial n} + n_y \frac{\partial \phi_y}{\partial n} + n_z \frac{\partial \phi_z}{\partial n}. \quad (16)$$

Since ϕ satisfies Laplace's equation (1) and Green's second identity (14), so do ϕ_x , ϕ_y and ϕ_z can be calculated using the BIM.

Once $\partial^2 \phi / \partial n^2$ is found, the normal stress, T_{mm} , can be obtained using a backward Euler approximation⁵⁷ for Maxwell's constitutive equation (12), given by

$$De \left(\frac{T_{mm}(x(t), t) - T_{mm}(x(t - \Delta t), t - \Delta t)}{\Delta t} \right) + T_{mm}(x(t), t) = \frac{2(1 + C)}{Re} \frac{\partial^2 \phi}{\partial n^2}, \quad (17)$$

where the variable time step is chosen as

$$\Delta t = \frac{\Delta\phi}{\max \left| 1 + \frac{1}{2} |\nabla \phi|^2 - \varepsilon \left(\frac{V_0}{V} \right)^\zeta + \frac{2\kappa}{We} - \frac{2C}{Re} \frac{\partial^2 \phi}{\partial n^2} - T_{mm} \right|} \quad (18)$$

for some constant $\Delta\phi$ found experimentally.

The BIM is grid-free in the flow domain making it computationally efficient; thus, the approach has been used extensively in many bubble dynamics simulations. At each time step, the bubble surface and potential distribution on the surface are known. The tangential velocity on the bubble surface is computed from the gradient of the potential using a polynomial interpolation combined with a least squares method. An advanced Linear Algebra Package (LAPACK) is used to solve the linear system (14) with a seven-point Gaussian quadrature being used to integrate the off diagonal elements of the matrix of coefficients. The weak singularities that occur in Eq. (15) are dealt with via a change to polar coordinates.^{64,65} The remaining singularities are eliminated by adopting a 4π rule.⁶⁰ Solving the boundary integral equation (14) yields the normal velocity on the surface. The bubble surface and potential distribution are updated on the bubble surface using Eqs. (10) and (18), with a second-order Runge-Kutta scheme. The stress tensor component, T_{mm} , is then calculated using a backward Euler method. A variable time step (18) is chosen for accuracy and efficiency, with the maximum change of potential at each time step being dependent on constant $\Delta\phi$.^{23,66} A hybrid approach for the Lagrangian method and elastic mesh technique is implemented to maintain a high quality surface mesh throughout the simulations.⁵⁸

IV. VALIDATION

A. Comparison with the Rayleigh–Plesset equation

We first compare the predictions of our numerical model with the solution of the Rayleigh–Plesset equation (RPE) for a spherical bubble with radius $R(t)$ in a non-Newtonian fluid given by

$$R \frac{d^2 R}{dt^2} = \varepsilon \left(\frac{R_0}{R} \right)^{3\gamma} - 1 - \frac{3}{2} \left(\frac{dR}{dt} \right)^2 - \frac{2}{We R} - T_{nm}. \quad (19)$$

The microbubble has an initial radius of $R_0^* = 4.5 \mu\text{m}$, and a total number of 5494 nodes of the surface mesh are used.

As shown in Fig. 1, the BIM predictions agree excellently with the RPE for the bubble radius history over two oscillation cycles for a Deborah number of $De = 2.0$. A similar agreement has been found for $De = 0.0, 0.2,$ and 20.0 .

Figure 2 displays that an increase in the Deborah number results in a significant increase in the maximum radius of the bubble over the first oscillation from 0.8203 to 0.8616 and an even greater increase over the second oscillation from 0.7395 to 0.8615. This is due to more elastic energy being stored and released in the viscoelastic fluid for a larger Deborah number and less energy being lost due to viscosity. This is apparent from Eq. (17), because the model approaches the inviscid case as De increases. Similarly, an increase in De also significantly increases the oscillation period of the bubble.

B. Comparison with experiments

To evaluate the BIM model, we compare the computational results with experimental data,⁵⁵ for a laser beam generated bubble with maximum radius $R_m = 0.88 \text{ mm}$ at a right angled corner of $\alpha = \pi/2$. The stand-off distances from the near and far walls are $\gamma_N = 0.88$ and $\gamma_F = 1.08$, respectively. The dimensionless parameters of the fluid are given by $\varepsilon = 100$ and $\kappa = 1.4$, where $Re = 8.4 \times 10^3$,

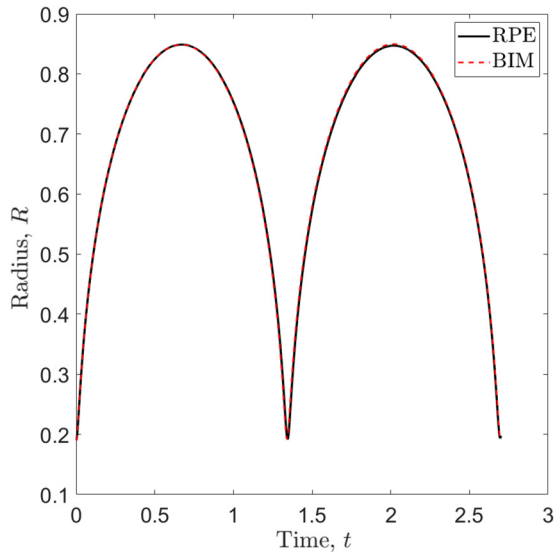


FIG. 1. The comparison of the radius history of a spherical bubble in a Maxwell fluid with $De = 2.0$, between the non-Newtonian Rayleigh–Plesset equation (RPE) (19) and the BIM code. The parameters of the surrounding liquid are $\zeta = 1.667$, $\sigma = 0.073 \text{ Nm}^{-1}$, $P_0 = 101.3 \text{ kPa}$, $P_v = 0.023 P_0$, and $\rho = 999 \text{ kgm}^{-3}$.

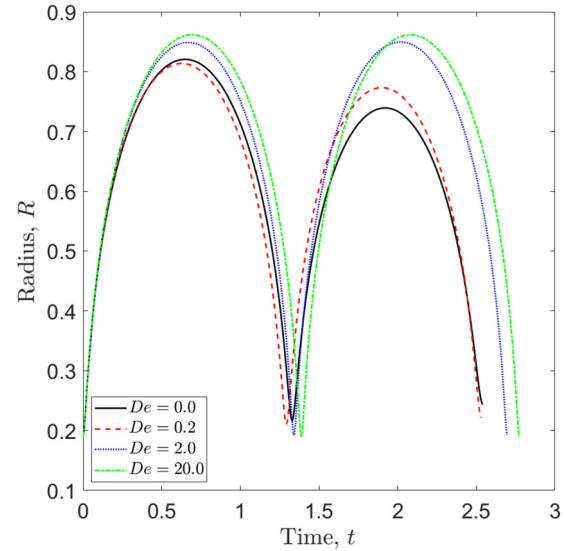


FIG. 2. The influence of De on the radius history of a spherical bubble in an infinite Maxwell fluid over the first two cycles of oscillation. The remaining parameters of the fluid are the same as in Fig. 1.

$We = 8.7 \times 10^{-3}$, and $\delta = 0.009$. As shown in Fig. 3, the bubble expands relatively spherical except for the flattening of the surface nearest the closer wall. Examining frames four and five, as the bubble collapses with the near wall surfaces remaining in contact with the walls, the distal surface collapses inwards and a jet begins to form. Finally, at collapse, a wide jet forms and penetrates the bubble surface pointing toward the corner. The BIM computations are in very good agreement with the experimental images.

C. Convergence test

To analyze the convergence of the BIM model, convergence tests were conducted for a bubble near a corner of angles $\alpha = \pi/2$ and $\pi/4$. As shown in Fig. 4, the jet profiles for numbers of elements $M = 5412$ and $M = 5724$ are excellent in both cases. As such, all the remaining calculations in this study are performed using $M = 5412$.

V. NUMERICAL RESULTS

First, we look at the evolution of a microbubble near corners of angle $\alpha = \pi/2$ and $\alpha = \pi/4$ in a Maxwell fluid with Deborah number

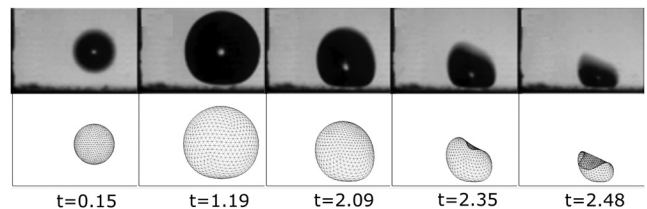


FIG. 3. Comparison for the evolution of a bubble in a corner between the BIM code and experimental data in a Newtonian fluid, with parameters $R_m^* = 0.85 \text{ mm}$, $\alpha = \pi/2$, $\gamma_F = 2.17$, $\gamma_N = 1.08$, $\varepsilon = 100$, and $\zeta = 1.4$, where $Re = 8.4 \times 10^3$, $We = 8.7 \times 10^{-3}$, and $\delta = 0.009$.⁵⁵

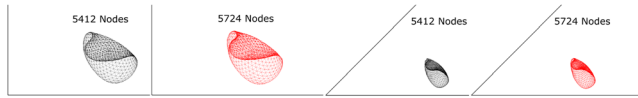


FIG. 4. The jet profiles and location of a bubble initiated with 5412 nodes and 5724 nodes for angles $\pi/2$ and $\pi/4$ with the remaining parameters being the same as in Fig. 1.

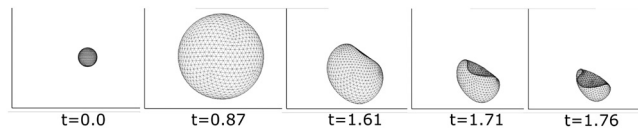


FIG. 5. The evolution of a three-dimensional bubble near a corner of angle $\alpha = \pi/2$ in a Maxwell fluid for $De = 2.0$ with the remaining parameters being the same as in Fig. 1.

$De = 2.0$. The stand-off distances are given by $\gamma_N = 1.0$ for the nearer horizontal wall below the bubble and $\gamma_F = 1.5$ for the further vertical wall to the left of the bubble. As shown in Fig. 5, the bubble expands approximately spherically until it reaches its maximum volume at $t = 0.87$. Due to the Bjerknes forces from the two rigid walls, the majority of the non-spherical collapse occurs on the side of the bubble furthest away from the corner. So, as the jet starts to form at $t = 1.61$, the sides of the bubble nearest to the walls remain relatively spherical while the side furthest from the corner becomes flatter. Note that there is more flattening on the side of the bubble closest to the far wall as opposed to the side of the bubble closest to the near wall. The collapse continues in this fashion until the bubble becomes toroidal at $t = 1.76$ with the jet rotated toward the far wall. As can be seen, the bubble has migrated toward the near wall with the bottom of the bubble remaining nearly spherical.

Figure 6 shows the evolution of a bubble in a Maxwell fluid near a corner of angle $\alpha = \pi/4$. The evolution is similar to the bubble near a corner of angle $\pi/2$ with the collapse occurring mostly on the bubble surface furthest away from the corner, and the jet rotated toward the far wall. Note the increase in the oscillation period is from 1.76 to 1.96.

We consider the shape of the bubble profile in a right-angled corner at collapse. The jet shapes are given in Fig. 7 for $De = 0.0, 0.2, 2.0,$ and 20.0 , with the black lines below and to the left side of the bubbles representing the location of the rigid boundaries of the corner. The jet shape is broader, and the bubble is much larger as the Deborah number increases. This is a result of the higher maximum radius as De increases, as there is a greater Bjerknes attraction between the bubble and the nearest wall below the bubble. This is apparent from the fact that the bottom of the bubble is much closer to the near wall as the Deborah number increases. Furthermore, because of this Bjerknes forces of attraction, the jetting

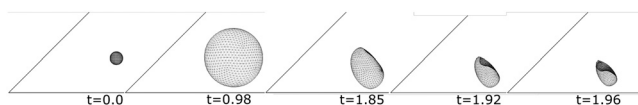


FIG. 6. The evolution of a three-dimensional bubble near a corner of angle $\alpha = \pi/4$ in a Maxwell fluid for $De = 2.0$ with the remaining parameters being the same as in Fig. 1.

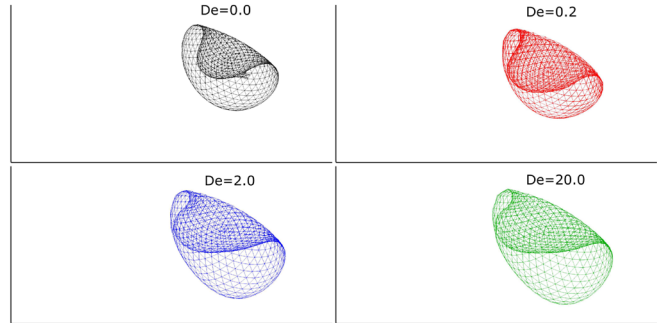


FIG. 7. The influence of De on the jet profiles and location of a bubble initiated in a corner of angle $\alpha = \pi/2$, with the remaining parameters being the same as in Fig. 1.

angle is more toward the far wall to the left as the Deborah increases, with a more asymmetric profile overall, as the jet becomes more angled.

The bubble profile at collapse for a corner of angle $\alpha = \pi/4$ is provided in Fig. 8. As shown, the collapse follows a similar trend for $\alpha = \pi/2$. As the Deborah number increases, the jet is broader and the bubble collapses closer to the nearer boundary. Once again, the jet is rotated upwards toward the far wall, an effect that is more apparent here given the restricted domain size.

The Kelvin impulse for a bubble is defined by

$$I(t) = \oint_{S_B} \phi n dS. \tag{20}$$

The Kelvin impulse corresponds to apparent inertia of the bubble, and its direction indicates the direction of bubble migration and jetting.^{67,68}

The Kelvin impulse toward the near and far boundaries over the first oscillation and subsequent bubble collapse is given, respectively, in Figs. 9 and 10 for $De = 0.0, 0.2, 2.0,$ and 20.0 . As shown, an increase in the Deborah number results in a large increase in the absolute value of the Kelvin impulse and, therefore, corresponds to a higher apparent inertia toward both boundaries.

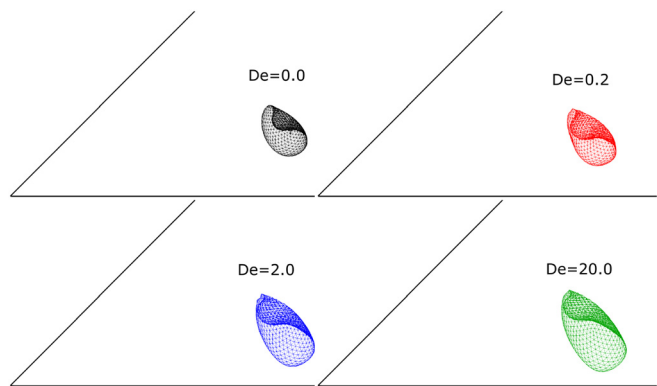


FIG. 8. The influence of De on the jet profiles and location of a bubble initiated in a corner of angle $\alpha = \pi/4$, with the remaining parameters being the same as in Fig. 1.

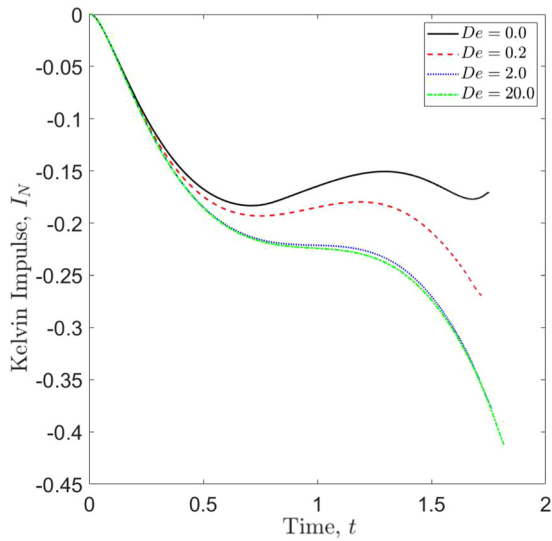


FIG. 9. The influence of De on the Kelvin impulse toward the near wall, for a bubble near a corner of angle $\alpha = \pi/2$ with $\gamma_N = 1.0$ and $\gamma_F = 1.5$. The remaining parameters are the same as in Fig. 1.

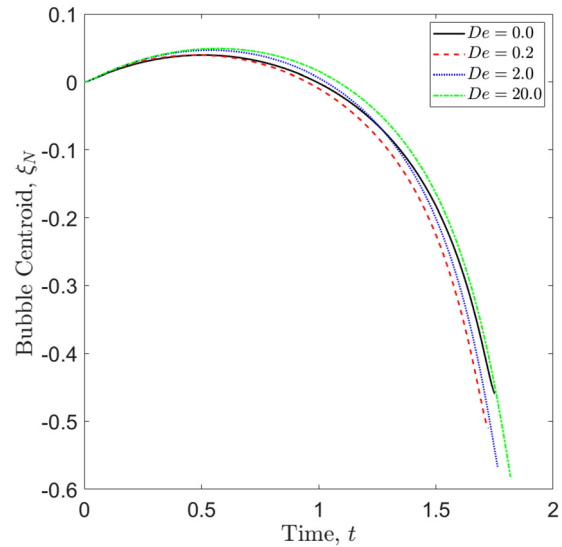


FIG. 11. The influence of De on the bubble centroid toward the near wall, for a bubble near a corner of angle $\alpha = \pi/2$ with $\gamma_N = 1.0$ and $\gamma_F = 1.5$. The remaining parameters are the same as in Fig. 1.

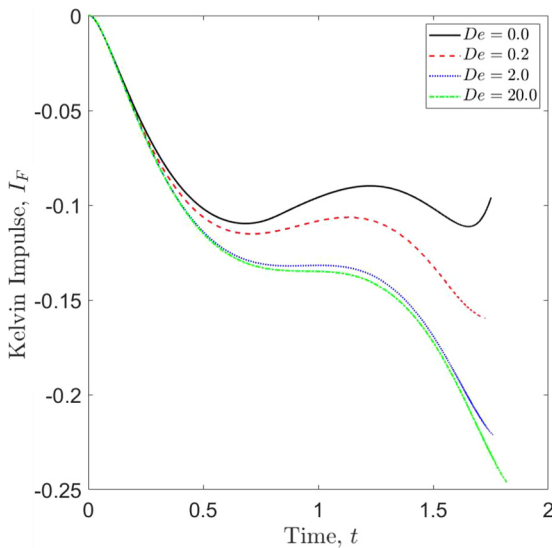


FIG. 10. The influence of De on the Kelvin impulse toward the far wall, for a bubble near a corner of angle $\alpha = \pi/2$ with $\gamma_N = 1.0$ and $\gamma_F = 1.5$. The remaining parameters are the same as in Fig. 1.

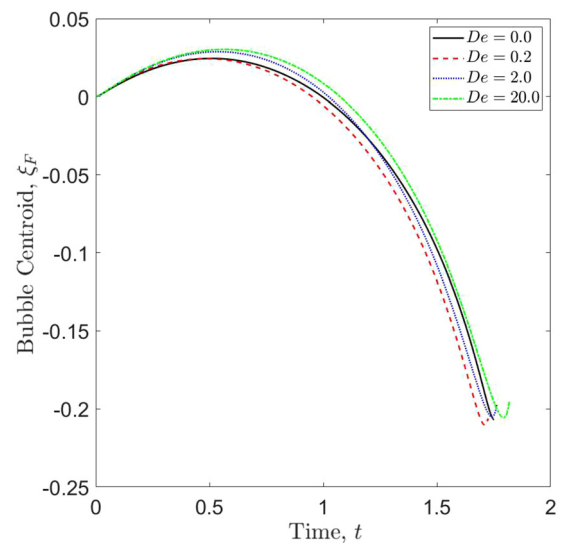


FIG. 12. The influence of De on the bubble centroid toward the far wall, for a bubble near a corner of angle $\alpha = \pi/2$ with $\gamma_N = 1.0$ and $\gamma_F = 1.5$. The remaining parameters are the same as in Fig. 1.

We now consider bubble migration toward both boundaries in the corner. The bubble centroid migration toward the near boundary is shown in Fig. 11. As shown, an increase in the Deborah number results in a greater migration of the bubble toward the near boundary. This point is apparent from Fig. 7 where it is clear that the bubble is closer to the near boundary at collapse as De increases. There is also the bubble migration toward the far wall. This is shown in Fig. 12. As can be seen, there appears to be not much of a difference between the bubble migration in this direction and what was seen in the direction

toward the near wall. This is because the bubble centroid motion toward the far wall is comparable in all cases due to the bubble being larger as the Deborah number increases. Note from Fig. 7 that indeed the left hand side of the bubble is closer to the vertical wall, but so also the right hand side of the bubble is further away as the Deborah number increases. So the bubble centroid in this direction is roughly similar for all Deborah numbers.

Figure 13 compares the equivalent bubble radius histories for $\alpha = \pi/2$ and $\alpha = \pi/4$ for $De = 0.0$ and 20.0 . The maximum bubble

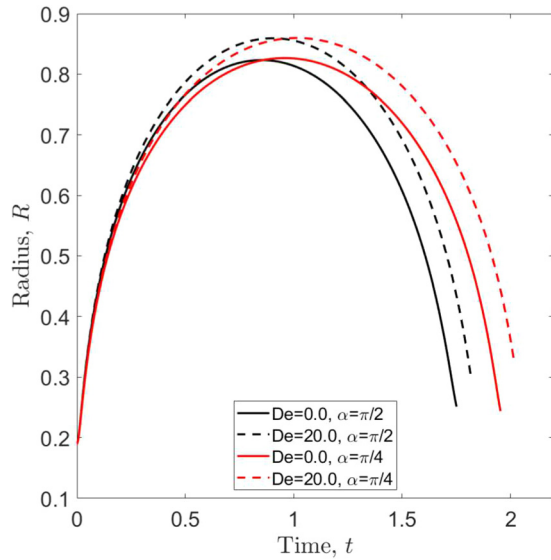


FIG. 13. The evolution of the bubble radius in an corner of angle $\alpha = \pi/2$ (black) and $\alpha = \pi/4$ (red) with $De = 0.0$ and 20.0 with the remaining parameters being the same as in Fig. 1.

radius and oscillation period increase with De . As α increases, the amplitude does not change significantly but the period decreases.

Figure 14 shows the jet shape for bubbles at collapse in viscoelastic fluids of Deborah number $De = 20.0$ and 200.0 . As shown, an increase from $De = 2.0$ to 20.0 results in a slightly larger bubble and a jet angle pointed more toward the far wall. However, increasing the Deborah number beyond $De = 20.0$ results in minimal change to the bubble profile at collapse. This can be seen by observing that the

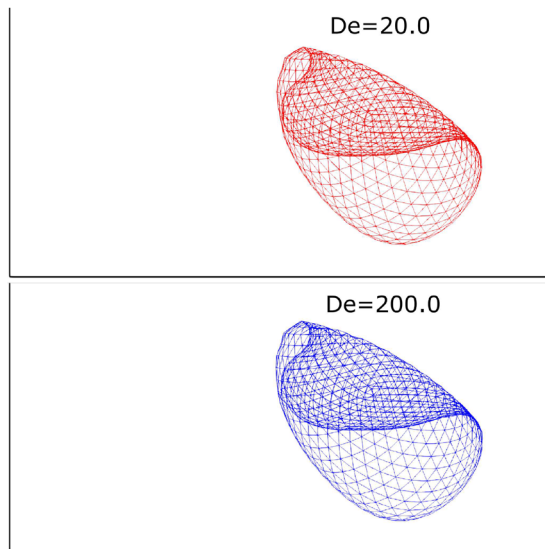


FIG. 14. The influence of large De on the jet profile, for a bubble near a corner of angle $\alpha = \pi/2$ with $\gamma_N = 1.0$ and $\gamma_F = 1.5$. The remaining parameters are the same as in Fig. 1.

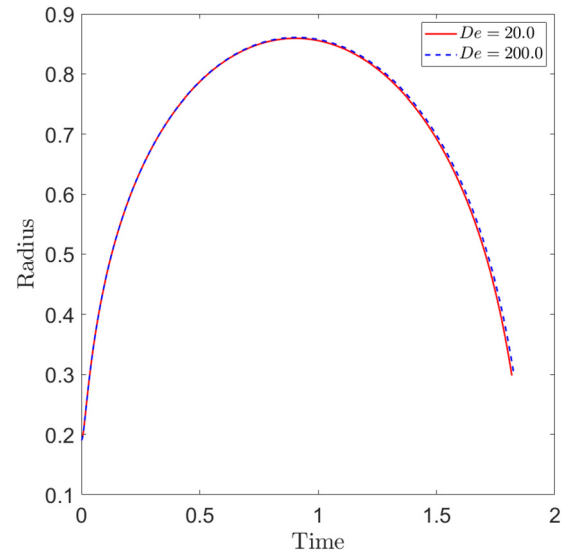


FIG. 15. The influence of large De on the radius history, for a bubble near a corner of angle $\alpha = \pi/2$ with $\gamma_N = 1.0$ and $\gamma_F = 1.5$. The remaining parameters are the same as in Fig. 1.

bubble profile for $De = 200.0$ has no significant difference from the bubble profile for $De = 20.0$. From Maxwell’s constitutive equation (12), we can see that DT_{mn}/Dt is inversely proportional to De . As De is large, DT_{mn}/Dt and T_{mn} are small and negligible. To see this, let us observe Eq. (12). As De increases, the Maxwell model converges to the non-viscous model where $T_{mn} \approx 0$ for all time.

Furthermore, Fig. 15 shows the corresponding radius history for the cases considered in Fig. 14. As shown, there is only a slight increase in the radius and oscillation period between $De = 20.0$ and $De = 200.0$.

VI. CONCLUSION

Bubble dynamics in non-Newtonian liquids has implications for a wide range of applications in engineering and biomedical ultrasonics. A numerical model is described based on the boundary integral method coupled with the Maxwell constitutive equation. Here, the flow is assumed to have high Reynolds number and thus is irrotational in the bulk domain. The viscoelastic effects are not negligible in a thin viscous layer at the bubble surface and are approximated only through the normal stress balance at the bubble surface. An Euler method is used to iteratively solve the Maxwell constitutive equation for the normal component of stress. Computations are carried out for a bubble near a corner for various corner angles using Green’s function for the Laplace equation in the corner domain.

The numerical model has been validated and excellent agreement with predictions obtained using the corresponding Rayleigh–Plesset equation for spherical bubbles in a non-Newtonian liquid is demonstrated. The numerical results also agree very well with experiments for bubbles in a Newtonian fluid near a corner. Viscoelastic effects are studied in terms of Deborah number De , which is as the ratio of the time it takes for a material to adjust to applied stresses to the characteristic bubble oscillation time. Simulations were performed for $De = 0.0$ (Newtonian fluid), $De = 0.02, 2.0, \text{ and } 20.0$ (viscoelastic fluid).

The following new phenomena/features were observed:

1. The maximum radius and oscillation period increase with the Deborah number. This is due to more elastic energy being stored and released in the viscoelastic fluid for a larger Deborah number and less energy being lost due to viscosity.
2. The wall effects due to the corner are enhanced with a larger De as a result of an increase in the maximum radius. Bubble migration and oscillation amplitude increase with the Deborah number.
3. The bubble jet shape is broader and flatter for a bubble near a rigid boundary or in a corner as De increases. The bubble jet is inclined to the further boundary when it is in a corner as De increases.
4. Results converge as the Deborah number increases as the elastic effects become dominant compared with the viscous damping effects of the fluid.

In conclusion, an increased Deborah number greatly enhances the effects of the surrounding boundaries on bubble collapse and provides a broader, flatter jet. This implies that a higher Deborah number in the fluid will enhance the interactions between a bubble and boundaries or other bubbles. This also suggests that, with certain parameter ranges, elasticity and non-Newtonian fluids may benefit ultrasonic cleaning, therapy, and drug delivery.

ACKNOWLEDGMENTS

This research was conducted under the funding of both the University of Birmingham and EPSRC (No. EP/S515292/1).

AUTHOR DECLARATIONS

Conflict of Interest

The authors have no conflicts to disclose.

Author Contributions

Eoin Nicholas O'Brien: Writing – original draft (lead). **Mehdi Hassan Mahmud:** Software (supporting). **Warren Robert Smith:** Supervision (supporting); Writing – review & editing (supporting). **Qianxi Wang:** Supervision (supporting); Writing – review & editing (supporting). **Timothy N. Phillips:** Methodology (supporting); Supervision (supporting); Writing – review & editing (supporting).

DATA AVAILABILITY

The data that support the findings of this study are available from the corresponding author upon reasonable request.

REFERENCES

- ¹U. Wisluff, R. Richardson, and A. Brubakk, "Exercise and nitric oxide prevent bubble formation: A novel approach to the prevention of decompression sickness?," *J. Physiol.* **555**, 825–829 (2004).
- ²T. Divoux, V. Vidal, M. Ripepe, and J. Géminard, "Influence of non-Newtonian rheology on magma degassing," *Geophys. Res. Lett.* **38**, 1–5, <https://doi.org/10.1029/2011gl047789> (2011).
- ³X. Frank, J. Charpentier, F. Canneviere, N. Midoux, and H. Li, "Bubbles in non-Newtonian fluids: A multiscale modeling," *Oil Gas Sci. Technol.–Rev. IFP Energies Nouvelles* **68**, 1059–1072 (2013).
- ⁴A. Ellis, "Some effects of macromolecules on cavitation inception and noise," Technical Report (California Inst of Tech Pasadena Div of Engineering and Applied Science, 1967).
- ⁵A. Shima, T. Tsujino, H. Nanjo, and N. Miura, "Cavitation damage in polymer aqueous solutions," *J. Fluids Eng.* **107**(1), 134–138 (1985).
- ⁶T. Tsujino, A. Shima, and H. Nanjo, "Effects of various polymer additives on cavitation damage," *Proc. Inst. Mech. Eng., Part C* **200**, 231–235 (1986).
- ⁷T. Tsujino, "Cavitation damage and noise spectra in a polymer solution," *Ultrasonics* **25**, 67–72 (1987).
- ⁸S. van der Meer, B. Dollet, M. Voormolen, C. Chin, A. Bouakaz, N. de Jong, M. Versluis, and D. Lohse, "Microbubble spectroscopy of ultrasound contrast agents," *J. Acoust. Soc. Am.* **121**, 648–656 (2007).
- ⁹S. Fong, E. Klaseboer, and B. Khoo, "Interaction of microbubbles with high intensity pulsed ultrasound," *J. Acoust. Soc. Am.* **123**, 1784–1793 (2008).
- ¹⁰Y. A. Pishchalnikov, O. A. Sapozhnikov, M. R. Bailey, J. Williams, Jr., R. Cleveland, T. Colonius, L. Crum, A. Evan, and J. McAteer, "Cavitation bubble cluster activity in the breakage of kidney stones by lithotripter shockwaves," *J. Endourol.* **17**, 435–446 (2003).
- ¹¹C. Coussios and R. Roy, "Applications of acoustics and cavitation to noninvasive therapy and drug delivery," *Annu. Rev. Fluid Mech.* **40**, 395–420 (2008).
- ¹²A. Carson, C. McTiernan, L. Lavery, A. Hodnick, M. Grata, X. Leng, J. Wang, X. Chen, R. Modzelewski, and F. Villanueva, "Gene therapy of carcinoma using ultrasound-targeted microbubble destruction," *Ultrasound Med. Biol.* **37**, 393–402 (2011).
- ¹³S. Kaul, "Microbubbles and ultrasound: A bird's eye view," *Trans. Am. Clin. Climatol. Assoc.* **115**, 137 (2004).
- ¹⁴K. Kooiman, M. Böhmer, M. Emmer, H. Vos, C. Chlon, W. Shi, C. Hall, S. de Winter, K. Schroën, M. Versluis *et al.*, "Oil-filled polymer microcapsules for ultrasound-mediated delivery of lipophilic drugs," *J. Controlled Release* **133**, 109–118 (2009).
- ¹⁵E. Brujan, A. Al-Hussany, R. Williams, and P. Williams, "Cavitation erosion in polymer aqueous solutions," *Wear* **264**, 1035–1042 (2008).
- ¹⁶H. Chmiel and E. Walitza, "On the rheology of human blood and synovial fluids," *Research Studies*, Chichester (1980).
- ¹⁷T. Annable, R. Buscall, R. Ettelaie, P. Shepherd, and D. Whittlestone, "Influence of surfactants on the rheology of associating polymers in solution," *Langmuir* **10**, 1060–1070 (1994).
- ¹⁸P. Fischer and H. Rehage, "Rheological master curves of viscoelastic surfactant solutions by varying the solvent viscosity and temperature," *Langmuir* **13**, 7012–7020 (1997).
- ¹⁹A. A. Ali and R. Makhloufi, "Linear and nonlinear rheology of an aqueous concentrated system of cetyltrimethylammonium chloride and sodium salicylate," *Phys. Rev. E* **56**, 4474 (1997).
- ²⁰M. E. Cates, "Flow behaviour of entangled surfactant micelles," *J. Phys.* **8**, 9167 (1996).
- ²¹J. Blake and D. Gibson, "Cavitation bubbles near boundaries," *Annu. Rev. Fluid Mech.* **19**, 99–123 (1987).
- ²²W. Lauterborn and T. Kurz, "Physics of bubble oscillations," *Rep. Prog. Phys.* **73**, 106501 (2010).
- ²³J. Blake, B. Taib, and G. Doherty, "Transient cavities near boundaries. Part 1. Rigid boundary," *J. Fluid Mech.* **170**, 479–497 (1986).
- ²⁴S. Zhang, J. Duncan, and G. Chahine, "The final stage of the collapse of a cavitation bubble near a rigid wall," *J. Fluid Mech.* **257**, 147–181 (1993).
- ²⁵Q. Wang, "The evolution of a gas bubble near an inclined wall," *Theor. Comput. Fluid Dyn.* **12**, 29–51 (1998).
- ²⁶A. Zhang and Y. Liu, "Improved three-dimensional bubble dynamics model based on boundary element method," *J. Comput. Phys.* **294**, 208–223 (2015).
- ²⁷E. Klaseboer, B. Khoo, and K. Hung, "Dynamics of an oscillating bubble near a floating structure," *J. Fluids Struct.* **21**, 395–412 (2005).
- ²⁸Y. Liu, Q. Wang, S. Wang, and A. Zhang, "The motion of a 3D toroidal bubble and its interaction with a free surface near an inclined boundary," *Phys. Fluids* **28**, 122101 (2016).
- ²⁹A. Zhang, W. Wu, Y. Liu, and Q. Wang, "Nonlinear interaction between underwater explosion bubble and structure based on fully coupled model," *Phys. Fluids* **29**, 082111 (2017).
- ³⁰K. Manmi and Q. Wang, "Acoustic microbubble dynamics with viscous effects," *Ultrason. Sonochem.* **36**, 427–436 (2017).
- ³¹Q. Wang, W. Liu, C. Corbett, and W. Smith, "Microbubble dynamics in a viscous compressible liquid subject to ultrasound," *Phys. Fluids* **34**, 012105 (2022).

- ³²S. Popinet and S. Zaleski, "Bubble collapse near a solid boundary: A numerical study of the influence of viscosity," *J. Fluid Mech.* **464**, 137–163 (2002).
- ³³V. Minsier, J. De Wilde, and J. Proost, "Simulation of the effect of viscosity on jet penetration into a single cavitating bubble," *J. Appl. Phys.* **106**, 084906 (2009).
- ³⁴C. Hsiao, A. Jayaprakash, A. Kapahi, J. Choi, and G. Chahine, "Modelling of material pitting from cavitation bubble collapse," *J. Fluid Mech.* **755**, 142–175 (2014).
- ³⁵G. Chahine, A. Kapahi, J. Choi, and C. Hsiao, "Modeling of surface cleaning by cavitation bubble dynamics and collapse," *Ultrason. Sonochem.* **29**, 528–549 (2016).
- ³⁶Q. Zeng, S. Gonzalez-Avila, R. Dijkink, P. Koukouvinis, M. Gavaises, and C. D. Ohl, "Wall shear stress from jetting cavitation bubbles," *J. Fluid Mech.* **846**, 341–355 (2018).
- ³⁷S. Kim, K. Lim, and C. Kim, "Deformation characteristics of spherical bubble collapse in Newtonian fluids near the wall using the finite element method with ale formulation," *Korea-Aust. Rheol. J.* **18**, 109–118 (2006).
- ³⁸C. Chen, Y. Gu, J. Tu, X. Guo, and D. Zhang, "Microbubble oscillating in a microvessel filled with viscous fluid: A finite element modeling study," *Ultrasonics* **66**, 54–64 (2016).
- ³⁹A. Wagner, L. Giraud, and C. Scott, "Simulation of a cusped bubble rising in a viscoelastic fluid with a new numerical method," [arXiv:cond-mat/9904029](https://arxiv.org/abs/cond-mat/9904029) (1999).
- ⁴⁰S. Lind and T. Phillips, "The effect of viscoelasticity on a rising gas bubble," *J. Non-Newtonian Fluid Mech.* **165**, 852–865 (2010).
- ⁴¹S. Lind and T. Phillips, "The effect of viscoelasticity on the dynamics of gas bubbles near free surfaces," *Phys. Fluids* **25**, 022104 (2013).
- ⁴²J. Liu, C. Zhu, T. Fu, Y. Ma, and H. Li, "Numerical simulation of the interactions between three equal-interval parallel bubbles rising in non-Newtonian fluids," *Chem. Eng. Sci.* **93**, 55–66 (2013).
- ⁴³W. Yuan, M. Zhang, B. Khoo, and N. Phan-Thien, "Dynamics and deformation of a three-dimensional bubble rising in viscoelastic fluids," *J. Non-Newtonian Fluid Mech.* **285**, 104408 (2020).
- ⁴⁴M. Niethammer, G. Brenn, H. Marschall, and D. Bothe, "An extended volume of fluid method and its application to single bubbles rising in a viscoelastic liquid," *J. Comput. Phys.* **387**, 326–355 (2019).
- ⁴⁵W. Yuan, M. Zhang, B. Khoo, and N. Phan-Thien, "On peculiar behaviours at critical volumes of a three-dimensional bubble rising in viscoelastic fluids," *J. Non-Newtonian Fluid Mech.* **293**, 104568 (2021).
- ⁴⁶D. Fragedakis, M. Pavlidis, Y. Dimakopoulos, and J. Tsamopoulos, "On the velocity discontinuity at a critical volume of a bubble rising in a viscoelastic fluid," *J. Fluid Mech.* **789**, 310–346 (2016).
- ⁴⁷S. Lind and T. Phillips, "Spherical bubble collapse in viscoelastic fluids," *J. Non-Newtonian Fluid Mech.* **165**, 56–64 (2010).
- ⁴⁸D. Joseph and J. Wang, "The dissipation approximation and viscous potential flow," *J. Fluid Mech.* **505**, 365–377 (2004).
- ⁴⁹D. Joseph and T. Liao, "Potential flows of viscous and viscoelastic fluids," *J. Fluid Mech.* **265**, 1–23 (1994).
- ⁵⁰R. Bird, R. Armstrong, and O. Hassager, "Dynamics of polymeric liquids, Volume 1: Fluid mechanics," *J. Non-Newtonian Fluid Mech.* **30**, 204–207 (1987).
- ⁵¹S. J. Lind and T. N. Phillips, "The influence of viscoelasticity on the collapse of cavitation bubbles near a rigid boundary," *Theor. Comput. Fluid Dyn.* **26**, 245–277 (2012).
- ⁵²E. Brujan, C.-D. Ohl, W. Lauterborn, and A. Philipp, "Dynamics of laser-induced cavitation bubbles in polymer solutions," *Acta Acust. Acust.* **82**, 423–430 (1996).
- ⁵³G. Chahine and D. Fruman, *Dilute Polymer Solution Effects on Bubble Growth and Collapse* (École Nationale Supérieure de Techniques Avancées Bretagne, 1979).
- ⁵⁴R. Owens and T. Phillips, *Computational Rheology*, Vol. 14 (Imperial College Press London, 2002).
- ⁵⁵E. Brujan, T. Noda, A. Ishigami, T. Ogasawara, and H. Takahira, "Dynamics of laser-induced cavitation bubbles near two perpendicular rigid walls," *J. Fluid Mech.* **841**, 28–49 (2018).
- ⁵⁶J. Blake, G. Keen, R. Tong, and M. Wilson, "Acoustic cavitation: The fluid dynamics of non-spherical bubbles," *Philos. Trans. R. Soc., A* **357**, 251–267 (1999).
- ⁵⁷S. Lind, "A numerical study of the effect of viscoelasticity on cavitation and bubble dynamics," Ph.D. thesis (Cardiff University, 2010).
- ⁵⁸Q. Wang and K. Manmi, "Three dimensional microbubble dynamics near a wall subject to high intensity ultrasound," *Phys. Fluids* **26**, 032104 (2014).
- ⁵⁹Y. L. Zhang, K. S. Yeo, B. C. Khoo, and C. Wang, "3D jet impact and toroidal bubbles," *J. Comput. Phys.* **166**, 336–360 (2001).
- ⁶⁰Q. Wang, "Unstructured mesh modelling of nonlinear unsteady ship waves," *J. Comput. Phys.* **210**, 368–385 (2005).
- ⁶¹A. Kucera and J. Blake, "Approximate methods for modelling cavitation bubbles near boundaries," *Bull. Aust. Math. Soc.* **41**, 1–44 (1990).
- ⁶²Y. Tagawa and I. Peters, "Bubble collapse and jet formation in corner geometries," *Phys. Rev. Fluids* **3**, 081601 (2018).
- ⁶³Q. Wang, M. Mahmud, J. Cui, W. Smith, and A. Walmsley, "Numerical investigation of bubble dynamics at a corner," *Phys. Fluids* **32**, 053306 (2020).
- ⁶⁴Z. Li, L. Sun, Z. Zong, and J. Dong, "Some dynamical characteristics of a non-spherical bubble in proximity to a free surface," *Acta Mech.* **223**, 2331–2355 (2012).
- ⁶⁵S. A. Wilkerson, *A Boundary Integral Approach to Three-Dimensional Underwater Explosion Bubble Dynamics* (The Johns Hopkins University, 1990).
- ⁶⁶J. Blake, B. Taib, and G. Doherty, "Transient cavities near boundaries part 2. free surface," *J. Fluid Mech.* **181**, 197–212 (1987).
- ⁶⁷J. Blake, D. Leppinen, and Q. Wang, "Cavitation and bubble dynamics: The Kelvin impulse and its applications," *Interface Focus* **5**, 20150017 (2015).
- ⁶⁸J. Blake, "The Kelvin impulse: Application to cavitation bubble dynamics," *ANZIAM J.* **30**, 127–146 (1988).